Climate Dynamics (2019) 53:3861–3875
https://doi.org/10.1007/s00382-019-04753-w

Role of SST feedback in the prediction of the boreal summer monsoon intraseasonal oscillation

Ying Zhang[1,2] · Meng-Pai Hung[3] · Wanqiu Wang[2] · Arun Kumar[2]

Received: 15 August 2018 / Accepted: 1 April 2019 / Published online: 15 May 2019

Abstract
This study investigates the impact of different specification of the underlying sea surface temperature (SST) on the prediction of intraseasonal rainfall variation associated with strong Monsoon Intraseasonal Oscillation (MISO) events in the northern Indian Ocean. A series of forecast experiments forced with observed hourly, daily, or seasonal SSTs are performed for three selected strong MISO events using the National Centers for Environmental Predictions (NCEP) atmospheric Global Forecast System (GFS). The comparison between these GFS forecasts shows that the intraseasonal SST variability is more important than its diurnal variability in the MISO prediction. The GFS experiments forced with daily SST which includes intraseasonal variability has higher prediction skill and faster speed in the northward propagation of the MISO intraseasonal rainfall anomalies than those forced with seasonal SST that do not include intraseasonal variability. No significant difference is found in the MISO prediction when GFS was forced by SST with or without SST diurnal cycle. The GFS runs forced with warmer and colder seasonal SSTs which mimic possible biases in SST prediction have comparable skill in the MISO prediction. A modified version of the NCEP Climate Forecast System coupled model (CFSm5) with 1- and 10-m vertical resolutions in the upper ocean is then used to examine their performance in the MISO prediction when all aspects of SST are actively included. The CFSm5 with 1-m vertical resolution in the upper ocean (CFSm501) shows larger amplitude of intraseasonal SST anomaly, with higher prediction skill in both intraseasonal SST and rainfall than the CFSm5 with the typical 10-m vertical resolution in the upper ocean (CFSm510) does. Compared with the uncoupled GFS, both CFSm501 and CFSm510, despite errors in predicted SSTs, have better prediction skill and more reasonable rainfall variability, which is attributed to the inclusion of active air–sea interaction. These results suggest the importance of intraseasonal variability of SST and air–sea interaction in improving the intraseasonal rainfall prediction associated with the MISO.

1 Introduction

The boreal summer monsoon intraseasonal oscillation (MISO; Suhas et al. 2013) is a dominant mode with a period of 10–90 days in the Indian monsoon region during boreal summer. The MISO is characterized by northward-propagating convection that originates from the equatorial Indian Ocean (Murakami 1976; Lau and Chan 1986; Wang and Rui 1990). As a notable aspect of the intraseasonal monsoon variability, the MISO regulates the onset, retreat, and the active and break phases of monsoon rainfall and associated wind fields and sea surface temperature (SST) disturbances over the Indian monsoon region and the mei-yu regime over South China (Yasunari 1979, 1980; Krishnamurti and Ardanuy 1980; Krishnamurti and Subrahmanyam 1982; Goswami and Ajayamohan 2001). Hence, the MISO has a strong influence on weather-sensitive socioeconomic activities (e.g. agriculture) and development in South-East Asia (Webster et al. 1998; Gadgil and Rao 2000).

Theoretical and numerical studies have attempted to explain the formation of the northward propagating MISO. One group considers the MISO as a result of internal atmospheric dynamics. For example, based on numerical experiments Wang and Xie (1997) found that northward propagating convection was formed by the equatorial Rossby waves emanating from the equatorial convection. Lawrence and

✉ Wanqiu Wang
Wanqiu.Wang@noaa.gov

[1] ESSIC, University of Maryland, College Park, MD, USA

[2] NOAA/NWS/NCEP Climate Prediction Center, 5380 University Research Court, College Park, MD, USA

[3] Chinese Culture University, Taipei, Taiwan

Webster (2002) used intraseasonally (25–80 day) filtered outgoing longwave radiation (OLR) and found there existed both eastward and northward propagations of convection centers from the central equatorial Indian Ocean in the summer time.

The other group of studies attested that the air–sea interaction was an important factor responsible for the MISO formation. The interaction between atmosphere and ocean could impact the amplitude, frequency and northward propagation of the MISO. Krishnamurti et al. (1988) showed the intraseasonal variation in the observational SSTs and wind speeds controlled the intraseasonal fluctuation in heat and moisture fluxes in the tropical Indian Ocean sector. Based on the satellite rainfall and reanalysis data, Roxy and Tanimoto (2007) indicated the processes contributing to the formation of intraseasonal rainfall: (1) suppressed surface latent heat flux and increased downward shortwave radiation flux resulted in the formation of positive SST anomalies, (2) the positive SST anomalies affected the surface air temperature anomalies, and destabilized the lower atmosphere, favoring convective activity and surface convergence.

In addition to observational evidence, a number of modeling studies also reveal the MISO is a coupled atmosphere–ocean phenomenon. Fu et al. (2003) indicated the northward propagating MISO was strongly coupled to underlying SST in two ways in the Indian Ocean based on a hybrid atmosphere–ocean coupled model. In their analysis, a coupled model was found to simulate stronger MISO and more realistic convection-SST relationship than its atmospheric-only component model (Fu and Wang 2004). Seo et al. (2007) confirmed the importance of air–sea interaction in numerical experiments with the National Centers for Environment Prediction (NCEP) coupled atmospheric-ocean Climate Forecast System (CFS). In addition, from a prediction perspective, inclusion of air–sea coupling should improve the simulation and prediction of the MISO and also extend its predictability. Fu et al. (2007, 2008) compared atmospheric-only and coupled experiments for MISO events and showed the MISO predictability was indeed extended when the interactive ocean was included.

The air–sea coupling is a two-way process and consists of atmospheric conditions associated with the MISO causing changes in the ocean and oceanic conditions feeding back to the atmosphere. Because SST is the oceanic variable that affects the atmosphere through fluxes, it is critical to understand the role of SST feedback in MISO variations. The relationship between SST and rainfall was documented by Klingaman et al. (2008b). The SST is attributed to as factor affecting destabilization of the lower troposphere and boundary layer convergence (DeMott et al. 2013). The importance of SST feedback in the prediction of MISO has been documented in previous studies; (e.g. Fu et al. 2003, 2007, 2008; Fu and Wang 2004; Roxy and Tanimoto 2007; Seo et al. 2007). A comprehensive analysis of the SST impact on surface fluxes and atmospheric moist static energy budget is given in DeMott et al. (2016), which is applied in MISO by Gao et al. (2018). Fu and Wang (2004) quantified that the AGCM forced with daily SSTs produced stronger MISO than that forced with monthly-mean SSTs. Similar results were obtained in Klingaman et al. (2008a) and Pegion and Kirtman (2008) who showed improved simulation of MISO with specifications of SSTs of higher frequencies. Wang et al. (2009) conducted experiments using NCEP atmospheric Global Forecast System (GFS) forced with prescribed SSTs and showed that the model produced MISO northward propagation speed, its amplitude and phase relationship between SST and rainfall strongly depended on the amplitude of the underlying SST anomalies. In addition to the importance of intraseasonal SST anomalies, the diurnal cycle is also suggested to have impact on the simulation of tropical intraseasonal variability (Seo 2014). The mean condition of SST has also been proposed as a factor that may affect the MISO variability (Inness et al. 2003; Li et al. 2016).

Diurnal SST variations have been analyzed in observational and modeling studies (Woolnough et al. 2007; Bellenger and Duvel 2009; de Szoeke et al. 2015; Ge et al. 2017). Woolnough et al. (2007) showed that intraseasonal SST anomalies are closely related to the variations of the amplitude in the SST diurnal cycle with positive (negative) intraseasonal SST anomalies corresponding to stronger (weaker) diurnal cycle during suppressed (active) convection phase, suggesting that a realistic simulation of intraseasonal SST variability in a numerical model requires correct representation of diurnal cycle. Ge et al. (2017) demonstrated that an oceanic general circulation model (OGCM) with a commonly-used vertical resolution (10 m) in the upper ocean underestimated SST diurnal as well as intraseasonal variability which was significantly improved with a 1-m vertical resolution in the upper ocean. The need for SST diurnal cycle with high vertical resolution in ocean to improve the simulation of tropical intraseasonal SST and Madden–Julian Oscillation (MJO) has also been investigated in Bernie et al. (2007, 2008), Klingaman et al. (2011) and Tseng et al. (2014).

The goal of this study is to assess the relative importance of different aspects of SST conditions in the intraseasonal rainfall prediction during the MISOs. Specifically, we address the following questions: (1) does the inclusion of SST diurnal cycle in SST anomalies result in a significant improvement in MISO predictions? (2) does the change of mean SST state (to mimic SST biases in coupled prediction) have any impact on the predicted MISOs? and (3) does the use of a higher vertical resolution in the upper ocean in a coupled model improve MISO prediction? This paper is organized as follows: the models and experimental design

are described in Sect. 2; the role of different specification of SST in the MISO prediction are analyzed in Sect. 3; the performance of coupled atmospheric-oceanic model in the MISO prediction are illustrated in Sect. 4; and a discussion and summary are provided in Sect. 5.

2 The model and experiments

2.1 The model

In this study, a modified version of Climate Forecast System version 2 (CFSv2) (Saha et al. 2014), CFSm5, is used for forecast experiments. Instead of the 2007 version of NCEP operational atmospheric GFS coupled with the Geophysical Fluid Dynamics Laboratory (GFDL) Modular Ocean Model (MOM) version 4 in CFSv2, CFSm5 consists of the 2011 version of GFS as its atmospheric component and MOM version 5 (MOM5; Griffies 2012) as its oceanic component. The two components in the CFSm5 exchange surface momentum, heat, and freshwater fluxes and SSTs every 30 min.

The GFS uses a T126 horizontal resolution and 64 vertical levels. The model physics is configured as in Saha et al. (2014), except for the use of the Relaxed Arakawa–Schubert (RAS) cumulus convection (Moorthi and Suarez 1992, 1999) instead of the Simplified Arakawa–Schubert (SAS) cumulus convection (Pan and Wu 1995). The choice of the RAS cumulus convection scheme is based on a few recent studies. Wang et al. (2015) examined the impact of convection schemes on the MJO simulations and found that RAS resulted in better simulations of MJO events during DYNAMO intensive observation period from October 2011 to January 2012 compared to the use of other convection schemes. Zhu et al. (2017) compared the performance of the RAS and SAS convection schemes in CFSv2 in the simulation of MJO propagation across the Maritime Continent and found that CFSv2 with RAS produced more realistic MJO propagations.

The horizontal resolution in MOM5, the oceanic component of CFSm5, is fixed at 0.5° in the zonal direction but uneven in the meridional direction with 0.25° between 10°S and 10°N, gradually increasing from 0.25° to 0.5° between 10° and 30° in both hemispheres, and staying at 0.5° poleward of 30°S and 30°N. Two configurations are used for the vertical resolution. In one configuration, MOM510, a 10-m vertical resolution is used for the upper 220 m. The other configuration, MOM501, is the same as MOM510 except for the use of 1-m vertical resolution in the top 10 m. MOM510 represents the commonly used vertical resolution in most of the contemporary extended-range prediction models. Other details about ocean model physics can be found in Griffies (2012). The temperature of the top layer at 5 m in the MOM510 and 0.5 m in the MOM501 is taken as simulated SST as commonly defined in OGCMs and coupled general circulation models (CGCMs).

2.2 Observations and strong MISO events

Rainfall from the Climate Prediction Center (CPC) morphing technique (CMORPH) satellite retrieval (Joyce et al. 2004) and SST from the operational SST and sea ice analysis (OSTIA; Donlon et al. 2012) are used to select strong MISO events and to validate model results. Strong MISO events are selected from daily-mean CMORPH rainfall and OSTIA SST between 2003 and 2017. The intraseasonal anomalies of rainfall and SST are computed in the following steps: (1) average SST and rainfall in northern Indian Ocean (5°–20°N, 65°–95°E) for ocean points only; (2) compute climatology of SST and rainfall; (3) produce raw daily anomalies of the two variables; (4) compute interannual anomalies as 91-day running mean of the raw anomalies; and (5) derive intraseasonal anomalies by removing the interannual anomalies from the raw anomalies.

Three strong MISO cases are selected from 2015 to 2017 based on two criteria: (1) both SST and rainfall intraseasonal anomalies reach 1.7 standard deviation at their peaks, respectively; and (2) the peak of SST intraseasonal anomalies leads the peak of rainfall intraseasonal anomalies by 4–12 days. The evolutions of SST and rainfall anomalies for these three cases are shown in Fig. 1. For each selected case, the day of peak rainfall intraseasonal anomalies is defined as day 0. Day 0 of the three selected cases is 16 May 2016, 30 October 2015, and 16 June 2015, respectively. The reasons to focus on the events during 2015–2017 are (1) hourly SST from OSTIA (Donlon et al. 2012) is available for this period, allowing the use of observational estimate of SST diurnal cycle in our forecast experiments, and (2) the smaller number of events facilitates a large number of forecast experiments to study the potential influence of different aspects of SST conditions.

2.3 Forecast experiment design

A group of atmosphere-only GFS forecast experiments from the same atmospheric initial conditions but forced with different SST specifications based OSTIA observational skin temperature analysis are designed to investigate what aspect of SST forcing is important for the prediction of intraseasonal rainfall in the MISO events. These experiments are designed to study SST impacts of (1) diurnal cycle, (2) intraseasonal anomalies, and (3) mean conditions. Five types of surface forcing are created from OSTIA SST for the three selected strong MISO cases (Table 1): (1) hourly SST (SSThly); (2) daily-mean SST (SSTdly) averaged from hourly data; (3) seasonal SST

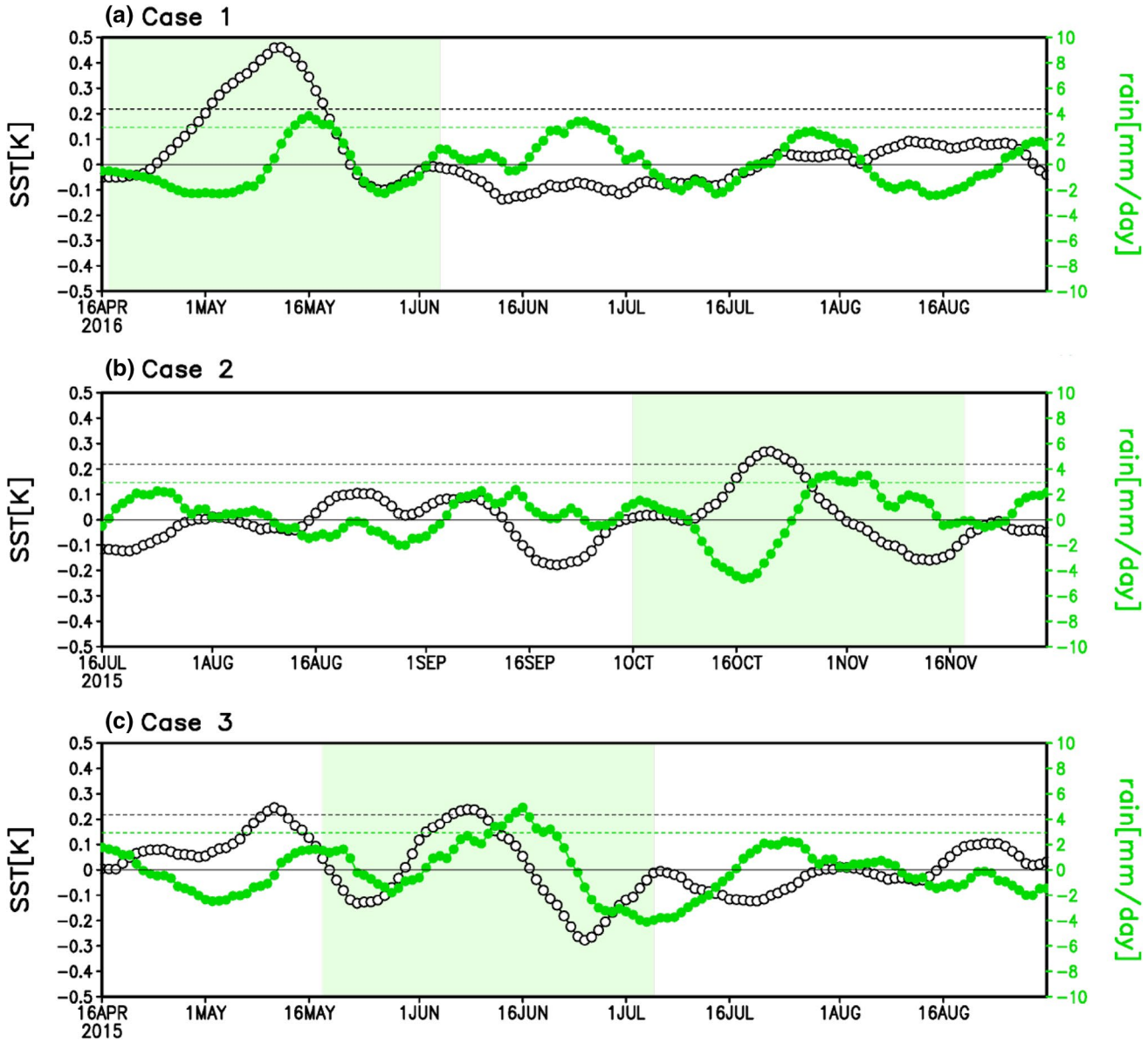

Fig. 1 Time evolution of intraseasonal anomalies of (5°–20°N, 65°–95°E) averaged CMORPH rainfall (black open circle lines) and OSTIA SST (green closed circle lines) for the three selected strong MISO cases. **a** Case 1, **b** case 2, and **c** case 3. The green shaded rectangles indicate initial dates for each case. The black and green dotted lines represent 1.7 standard deviation of SST and rainfall intraseasonal anomalies, respectively

Table 1 Forecast experiments

	Experiments	SST variability	SST forcing
GFS	SSThly	Hourly	Hourly OSTIA SST
	SSTdly	Daily	Daily OSTIA SST
	SSTssn	Seasonal	Daily OSTIA SST without intraseasonal variation
	SSTssnh	Warmer Seasonal	Daily OSTIA SST without intraseasonal variation + 1 K in the tropical Indian Ocean
	SSTssnl	Cooler Seasonal	Daily OSTIA SST without intraseasonal variation − 1 K in the tropical Indian Ocean
CFSm5	CFSm501	1 m vertical resolution in the upper ocean in MOM5	
	CFSm510	10 m vertical resolution in the upper ocean in MOM5	

(SSTssn) obtained by computing 91-day running mean of the daily SST over the tropical Indian Ocean [(30°S–31°N, 20°–100°E) and (30°S–0°, 100°–145°E)]; (4) higher seasonal SST (SSTssnh) computed by adding 1 K to the seasonal SST in (3) in the tropical Indian Ocean; (5) lower seasonal SST (SSTssnl) computed by reducing 1 K from the seasonal SST in (3) in the tropical Indian Ocean. Daily SST in (2) is used to force GFS outside the tropical Indian Ocean in (3), (4) and (5).

In addition to the atmosphere-only GFS experiments, two forecast experiments are carried out with the coupled CFSm5 with different configurations in the vertical resolution in the upper ocean, one with 10 m (CFSm510) and the other with 1 m (CFSm501). CFSm501 is expected to produce stronger SST diurnal cycle and intraseasonal anomalies according to the results from previous studies (Woolnough et al. 2007; Bernie et al. 2007; Ge et al. 2017) and may lead to enhanced skill in capturing the observed MJO evolution compared to the CFSm10.

All GFS and CFS forecast experiments are initialized daily from 00Z from Day −29 to Day +19 for each strong MISO event and integrated for 30 days. Initial conditions were taken from the Climate Forecast System Reanalysis (Saha et al. 2010). An ensemble of four forecast runs were made from each initial date with small perturbations to atmospheric initial conditions. The initial conditions used for the experiments were directly taken from that for operational CFSv2 forecasts. Construction of the perturbations was described in Saha et al. (2006, 2014). Initial state for each ensemble member is a weighted average of the analysis states corresponding to the forecast start date and a day earlier at 0000 UTC, which is equivalent to using a fraction of the one-day apart differences as the initial perturbations. Details of all forecast experiments are summarized in the Table 1.

2.4 Analysis method

Daily mean fields of four-member ensemble average are used for diagnoses. The intraseasonal anomaly of a field is computed for each experiment as the departure of the forecast field from a background state for each lead time. The background is defined as a linear fit over the 49-day initial date period (day −29 to day 19). This background state represents seasonal and interannual variability. For consistency, the corresponding observed anomalies for verification and skill assessment are also calculated in the same way by rearranging observations for each initial date and lead time. It is noted that this method to calculate observed anomalies is not the same as that used in Sect. 2.2 to define rainfall and SST anomalies that are used to select MISO events. Composite rainfall and SST anomalies for the three MISO cases are calculated for diagnoses and are validated against observations.

3 SST feedback to the MISO prediction

In this section, we analyze the role of different SST specifications in the GFS prediction of intraseasonal rainfall in the MISO events. The five groups of GFS forecast experiments with specified SSTs (Table 1) are assessed by comparing the statistics of rainfall intraseasonal anomalies correlations and the composite anomalies with the corresponding observations.

Because the intraseasonal time scale lies between the synoptic weather and seasonal climate, both atmospheric initial conditions and lower boundary conditions affect the predictability of MISO (Fu et al. 2007, 2009). Since atmospheric initial states for different experiments are the same, discrepancies in the intraseasonal forecasts among those GFS experiments are due to the difference in oceanic surface boundary conditions, i.e. the SST forcing. Specifically, differences in the forecast between GFS_SSThly and GFS_SSTdly indicate the importance of SST diurnal cycle in the MISO prediction; differences between GFS_SSTdly and GFS_SSTssn show the role of SST intraseasonal variability; and the comparison between GFS_SSTssn and GFS_SSTssnh (GFS_SSTssnl) test the sensitivity to warmer (colder) SST mean states.

3.1 Impacts of SST diurnal cycle and intraseasonal variation on the MISO prediction

The prediction skills of the intraseasonal rainfall anomaly for the three strong MISO events are examined in Fig. 2 by the temporal correlations of the northern Indian Ocean (5°–20°N, 65°–95°E)-averaged intraseasonal rainfall anomaly between GFS forecasts and CMORPH observation. The correlation skills of GFS forecasts forced with hourly SST (GFS SSThly) and daily SST (GFS_SSTdly) is comparable to each other and has no significant difference, especially for the first 17 days. This suggests that the prediction of intraseasonal precipitation anomaly in the strong MISO event is not sensitive to the diurnal cycle in the SST forcing.

The correlation skill of GFS_SSTdly is higher than that of the GFS forecasts forced with seasonal SST (GFS_SSTssn) for the lead time from 1 to 30 days and the difference becomes larger after 8 days when the influence of initial condition decays and the SST forcing becomes more important. The skill of GFS_SSTdly at the 11-day lead is similar to that at the 9-day lead in GFS_SSTssn, representing an improvement of around 2 days. This indicates

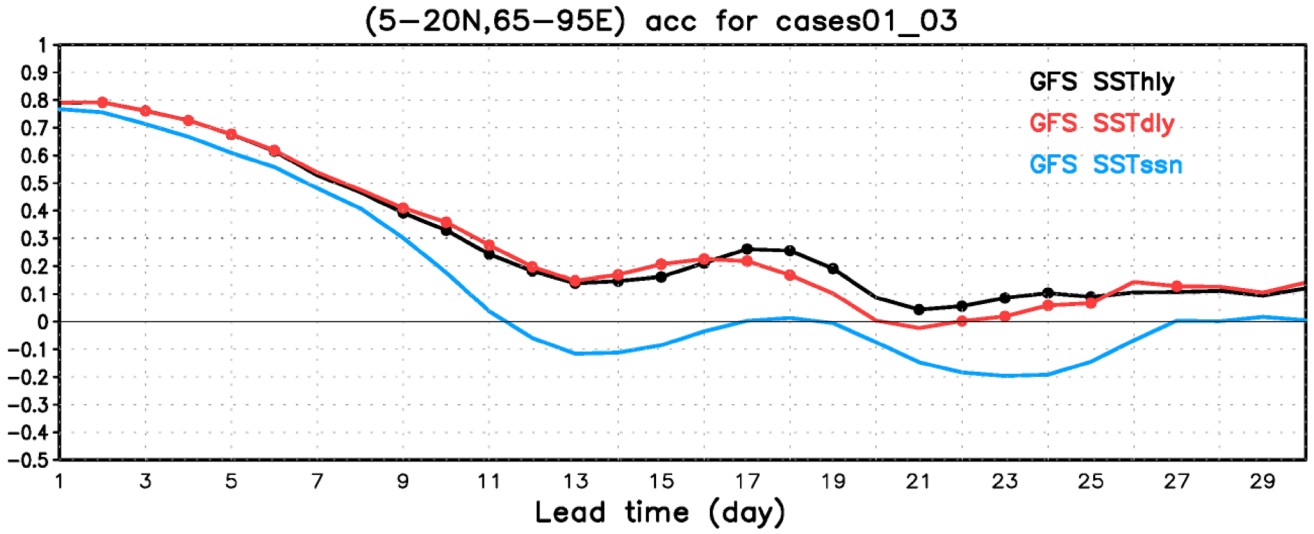

Fig. 2 Anomaly correlation of precipitation between CMORPH observations and GFS forecasts forced with hourly, daily, and seasonal OSTIA SST in (5°–20°N, 65°–95°E)

that the prediction of consistent intraseasonal SST variations is important to improve the intraseasonal rainfall forecast. As shown later, prediction skills in GFS_SSThly and GFS_SSTdly are lower than that in coupled model (CFSm5) predictions. The use of specified SST result in an unrealistic relationship among SST, precipitation, and latent heat flux (LHF) compared to the relationship in coupled model predictions and in observations. These inconsistent relationships among variables in uncoupled predictions are possible reasons for the lower skill in uncoupled predictions.

Relationships between rainfall and SST are presented in Fig. 3 based on composites of the three selected strong MISO events averaged between 65° and 95°E. Composites of observed CMORPH rainfall anomaly (shaded) and OSTIA SST anomaly (contours) are shown in Fig. 3a. The rainfall band starts from 5°S on Day −13, then moves northward to 7°N on Day −3, and accelerates to 20°N on Day 5. It is clear that this northward-moving rainfall band follows the northward-propagating warm SST anomaly, which starts from 5°S at Day −15 and then spreads northward to 25°N at Day 7. After Day −5, warm SST anomaly is located to the north of the rainfall band and cold SST anomaly exists to the south of the rainfall band. Negative rainfall anomaly then follows the cold SST anomaly and appears in the south of the equator. These SST and rainfall distribution are consistent with physical processes proposed by Kemball-Cook and Weare (2001) from the observations: warm sea surface increases the low-level convergence, destabilize the atmosphere and leads the equatorial convection to propagate northward.

Intraseasonal rainfall and SST anomalies in the Indian Ocean (65°E–95°E average) at 9-day lead from GFS_SSTdly and GFS_SSTssn runs are shown in Fig. 3b, c, respectively. Because GFS_SSTdly is forced with daily OSTIA skin temperature, SST anomalies from GFS_SSTdly output are similar to those in Fig. 3a with only small differences. The GFS_SSTssn forecast (Fig. 3c) shows little SST intraseasonal anomaly as expected. For the rainfall, both GFS forecast experiments capture the basic characteristics that the rainfall band propagates northward from 4°N to 20°N as presented in the observations, with the rainfall band located more southward than the CMORPH observation. The amount of rainfall forecasts is underestimated in the both GFS experiments. For example, both GFS forecasts miss the rainfall in 5°S—Equator from Day −12 to Day −4. The maximum rainfall rate reaches over 11 mm day^{-1} lasting from Day −1 to Day 5 in the CMORPH, comparing about 5–7 mm day^{-1} lasting from Day −1 to Day 4 in the GFS_SSTdly 9-day lead forecast, and about 5–7 mm day^{-1} lasting from Day 1 to Day 5 in the GFS_SSTssn 9-day lead forecast.

For the northward propagating speed of intraseasonal rainfall anomaly, GFS_SSTdly almost catches up the speed of CMORPH observations after Day −3, while GFS_SSTssn is a little slower than observations. It takes about 11 days for rainfall to move from 5°S to 7°N and 9 days from 7°N to 20°N in CMORPH observation, about 10 days from the Equator to 20°N in GFS_SSTdly forecast, and about 12 days from the Equator to 20°N in GFS_SSTssn forecast. Finer differences between GFS_SSTdly and GFS_SSTssn also can be seen with a close inspection. The positive rainfall anomalies between 18°N–20°N from Day 1 to Day 5 in GFS_SSTdly,

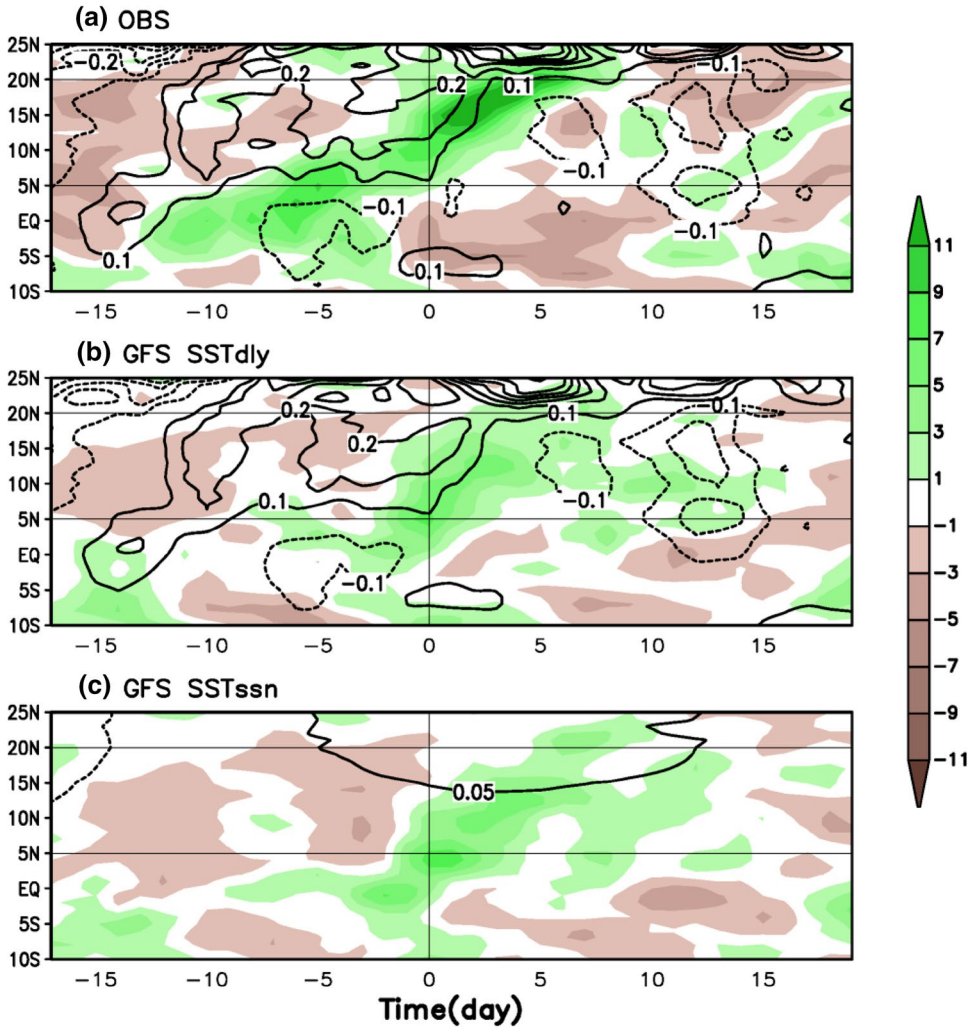

Fig. 3 Hovmoller plots of rainfall rate anomalies (unit: mm day^{-1}, shaded) and SST anomalies (unit: K, contour) averaged between 65° and 95°E from **a** observations and composite, **b** GFS SSTdly runs and **c** GFS SSTssn runs of the three strong MISO events at 09-day lead forecast

Table 2 Correlation and RMSE of precipitations

	GFS_SSTdly vs. OBS	GFS_SSTssn vs. OBS
Correlation	0.42	0.19
RMSE (mm day^{-1})	2.96	3.43

which are missing in GFS_SSTssn, are believed to be related to the leading SST warming anomalies. The continuation of positive rainfall anomalies in GFS_SSTssn between 15°N and 20°N after Day 10, which does not exist in GFS_SSTdly, is likely due to the lack of negative SST anomalies as in GFS_SSTdly. A more qualitative comparison of rainfall anomalies between GFS_SSTdly and GFS_SSTssn is made by calculating their correlation and root-mean-sqaure error (RMSE) against observations (Table 2). It is shown that the GFS capability in capturing the intraseasonal rainfall variability is decreased from 0.42 to 0.19 in correlation and increased in RMSE from 2.96 to 3.43 mm day^{-1}, when intraseasonal SST variability is removed for MISO forecasts.

To further analyze the SST-precipitation relationship between observations and GFS forecasts, temporal evolutions of rainfall and SST intraseasonal anomaly averaged over the northern Indian Ocean (5°–20°N, 65°–95°E) from 9-day lead GFS forecasts are compared with the corresponding CMORPH and OSTIA observations in Fig. 4. OSTIA SST anomaly evolves with a period of approximately 33 days measured from Day − 15 to Day 17 when the SST anomalies change from negative to positive values: It starts to increase and maintains positive during Day − 15 to Day 2 and then decrease to negative from Day 3 to Day 17. After OSTIA SST anomaly warms up, a positive CMORPH rainfall anomaly starts from Day − 6, increases to about maximum 7 mm day^{-1} at Day 1 and then decreases to 0 at Day 5 which follows the cooling down of SST anomaly. The precipitation forecast from GFS_SSTdly is generally in-phase with the CMORPH observations, although the maximum rate is only 4 mm day^{-1} at Day 1. The precipitation forecast

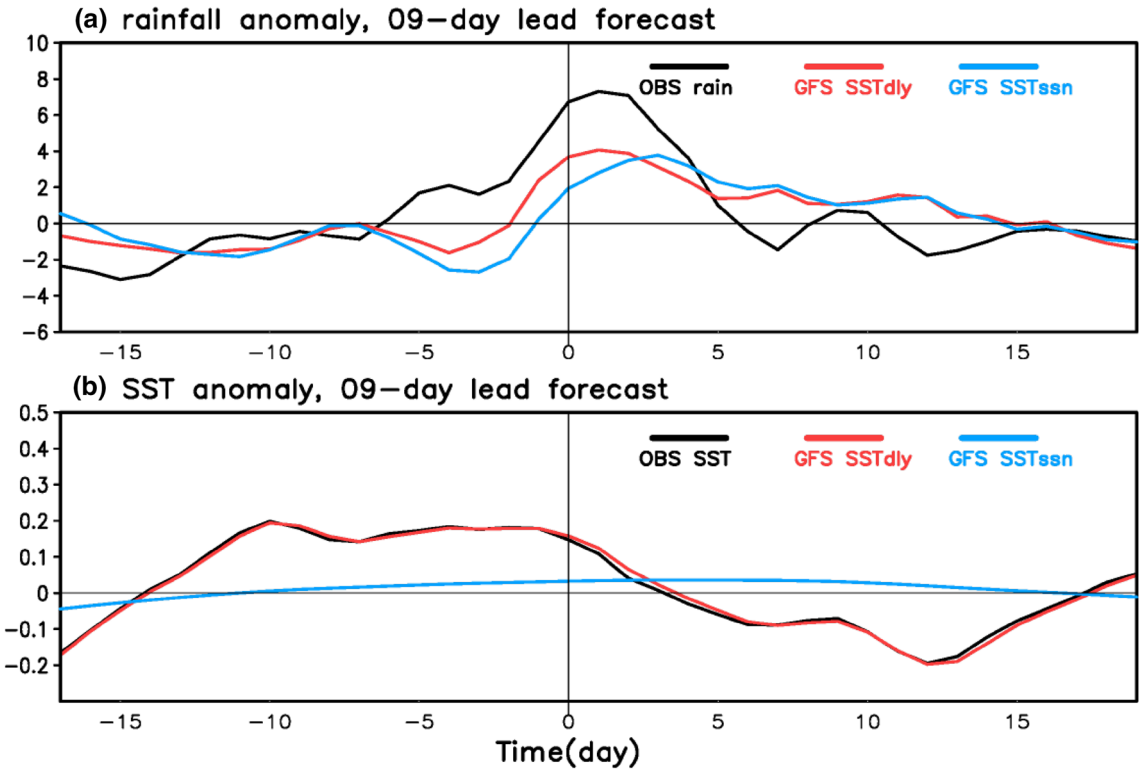

Fig. 4 Rainfall rate anomalies (unit: mm day^{-1}) and SST anomalies (unit: K) averaged over (5°–20°N, 65°–95°E) from observations (black) and composite GFS SSTdly runs (red) and GFS SSTssn runs (blue) of the three strong MISO events at 09-day lead forecast. **a** Rainfall anomaly; **b** SST anomaly

from GFS_SSTssn, which has the similar magnitude as the GFS_SSTdly forecast, lags the CMORPH observations in phase by approximately 2 days while the GFS_SSTdly follows the observation more closely.

Therefore, the magnitude and northward propagation of rainfall intraseasonal anomaly in the GFS_SSTdly forecasts overall is closer to the CMORPH observation than that in GFS_SSTssn forecasts. Considering that GFS_SSTdly and GFS_SSTssn are initialized from the same atmospheric initial states but are forced by different SST specifications, the difference in SST forcing, i.e., the existence of SST intraseasonal variability, determines the difference in the forecast of rainfall between the two GFS experiments after the effect of the atmospheric initial condition gradually declines. With intraseasonal variability in the daily SST forcing, GFS_SSTdly have better forecasts than GFS_SSTssn in the magnitude and northward propagation of MISO precipitation anomaly.

3.2 The impact of SST mean state on the MISO prediction

Another aspect of SST impacts is the role of mean SST state. Many CGCMs suffer from biases in simulating the tropical climate. For example, Davey et al. (2002) found mean state equatorial cold biases in the central Pacific in the majority of thirteen CGCMs without flux adjustment. Wang et al. (2014) showed generally warm (cold) annual mean SST biases in the Northern (Southern) Hemisphere in the most Coupled Model Intercomparison Project phase 5 (CMIP5) CGCMs and strong biases in the Pacific and Atlantic Oceans. Li et al. (2015) found that the multimodel ensemble-mean SST biases in CMIP5 CGCMs showed strong warm (weak cool) SST biases in the western (eastern) Indian Ocean in summer and fall seasons. Innes et al. (2003) suggested that a cold SST bias in the Western Pacific prevented MJO from propagating from Indian Ocean into the Western Pacific. In a recent study, Li et al. (2016) analyzed satellite observations and model experiments and found that high SST mean state (> 29 °C) in May–June could favor active air–sea interaction and enhance the response of MISO convection to SST anomaly. The hypothesis that the mean SST state might have an impact on MISO prediction is tested in this study by carrying out two GFS forecast experiments which are the same as GFS_SSTssn but with the seasonal SST increased (GFS_SSTssnh) or decreased (GFS_SSTssnl) by 1 K, to mimic the SST biases in coupled forecast.

The rainfall prediction anomaly correlation skill over the northern Indian Ocean (5°–20°N, 65°–95°E) of the three

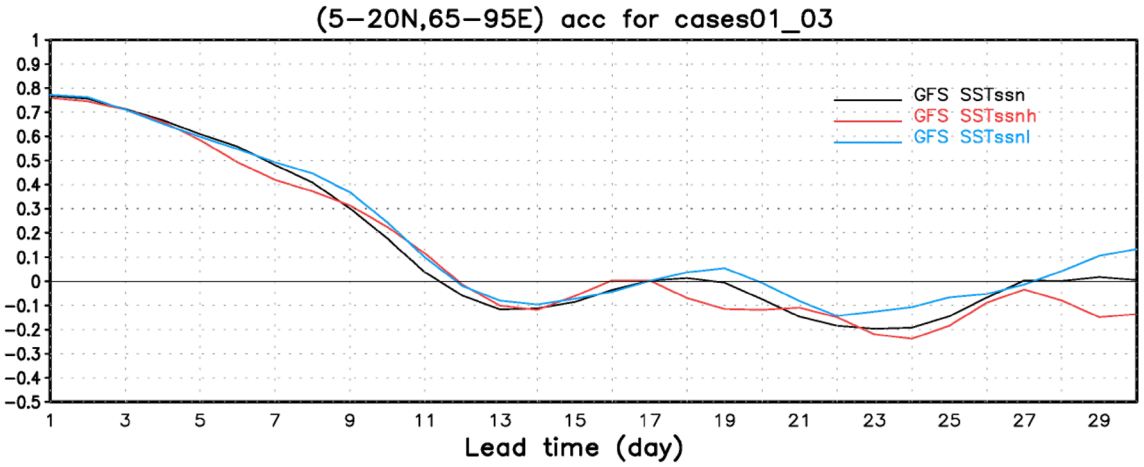

Fig. 5 Anomaly correlation of rainfall rate between CMOPRH observations and GFS forecast forced with seasonal OSTIA SST with different magnitudes in (5°–20°N, 65°–95°E)

groups of GFS experiments which are forced with seasonal SSTs that do not include intraseasonal variability is compared in Fig. 5. Initialized from the same atmospheric initial states, although SST forcing differs by 1 K (between GFS_SSTssn and GFS_SSTssnh and between GFS_SSTssn and GFS_SSTssnl), and 2 K (between GFS_SSTssnh and GFS_SSTssnl), the forecast skills of the three GFS runs are quite similar, with no significant difference among them for the lead time from 1 to 30 days. The details of northward propagating rainfall band from the three GFS forecasts (figures not shown) also show little differences among the three experiments. Therefore, with only seasonal variability in SST forcing, GFS intraseasonal rainfall forecasts over the northern Indian Ocean (5°–20°N, 65°–95°E) during the strong MISO events is not sensitive to the magnitude of the mean state of SST forcing.

In summary, among different time scales, variability in the intraseasonal period band in the underlying SST forcing is the most important factor to improve GFS intraseasonal rainfall forecast during the strong MISO events. The addition of SST diurnal cycle does not appear to be critical in the simulation of the MISO-associated rainfall variations. In addition, changes in the mean SST state alone also do not result in a significant change in the prediction of MISO-associated rainfall.

4 MISO prediction in CFSm5

The MISO has been demonstrated to be associated with air–sea coupling processes by a number of observational and numerical studies (e.g. Wang and Xie 1998; Fu et al. 2003, 2007, 2008). Inclusion of the two-way air–sea interaction in coupled models extended the predictability of MISO associated intraseasonal rainfall (e.g. Fu et al. 2007). After analyzing which specification of SST is important to the MISO prediction, another question is raised, i.e., how a coupled model performs when the SST variability on different time scales including diurnal cycle and intraseasonal variations is produced within the model. While the above analysis shows that diurnal cycle is not important in the forced atmosphere-only MISO simulation, it may be important for MISO simulations and predictions in a coupled atmosphere–ocean model which predicts the required SST as the boundary condition for the atmospheric component. The possibility comes from the fact that a realistic representation of intraseasonal SST variations in an oceanic model may strongly depend on whether the diurnal cycle is correctly simulated which requires a high-vertical resolution for the near-surface ocean (Woolnough et al. 2007; Ge et al. 2017).

To validate the possibility, two forecast experiments were carried out with the coupled CFSm5. Both experiments were initialized from the CFSR initial states as in the GFS experiments but using a 1-m (CFSm501) and 10-m (CFSm510) vertical resolution in the upper ocean for the oceanic component (Table 1). The prediction of CFSm5 intraseasonal SST is firstly validated by anomaly correlation against OSTIA observations over the northern Indian Ocean (5°–20°N, 65°–95°E) during the strong MISO events as presented in Fig. 6. The anomaly correlation of CFSm501 and CFSm510 SST is quite close for the lead time from 1 to 10 days, and the CFSm501 has higher correlation skill than the CFSm510 for most of the lead time starting after Day 11.

The benefits of high ocean vertical resolution for the prediction of intraseasonal rainfall are next analyzed with anomaly correlation (Fig. 7) for the intraseasonal precipitation anomalies over the northern Indian Ocean (5°–20°N, 65°–95°E). Overall, the CFSm501 has higher rainfall

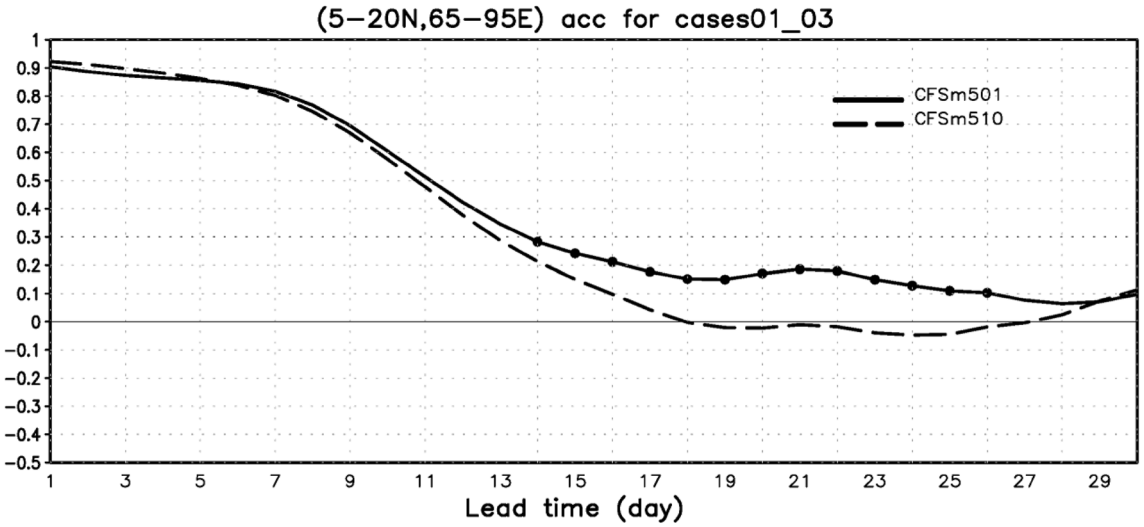

Fig. 6 Anomaly correlation of SST between CFSm5 forecasts and OSTIA observations in (5°–20°N, 65°–95°E)

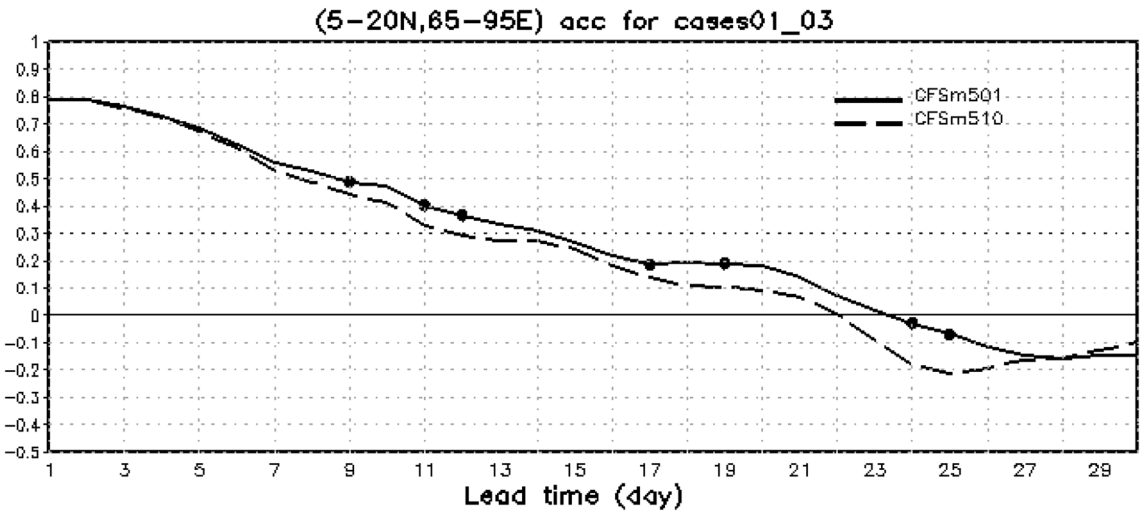

Fig. 7 Anomaly correlation of rainfall between CFSm5 forecasts and CMORPH observations in (5°–20°N, 65°–95°E)

prediction skill than the CFSm510 (Fig. 7). The correlation skill difference is consistent for most of the lead time after Day 7 although absolute value of the skill difference is small. The CFSm501 with high vertical resolution in the upper ocean extends the prediction of intraseasonal precipitation over the northern Indian Ocean (5°–20°N, 65°–95°E) for 3 days at the skill of 0.3.

The composites of 11-day lead forecasts of rainfall and SST from the CFSm501 (Fig. 8a) and CFSm510 (Fig. 8b) show similar patterns as observations (Fig. 3a): northward-propagating positive rainfall anomaly is preceded by northward-propagating warm SST anomaly from 5°S to north of 20°N. Unlike the GFS forecasts, both CFSm5 forecasts overall capture the slowly northward moving positive rainfall anomaly from 5°S to 7°N during Day − 13 to Day − 3 in the CMORPH observation. The rainfall band in the CFSm501 forecast moves at the similar speed as the observed. The development of positive rainfall anomalies between the Equator and 10 N before Day − 3 is better captured in CFSm501 than in CFSm510. After Day − 3, the northward propagation of the observational positive rainfall band accelerates; however, both CFSm5 forecasts do not catch up this acceleration and they even slow down after Day − 3 instead. It takes the CMORPH observation, CFSm501 forecast, and CFSm510 forecast 9, 11, and 12 days respectively to move from 7°N to 20°N. Both CFSm5 forecasts underestimate the magnitude of positive intraseasonal rainfall anomaly, with the maximum rainfall rate of 5 mm day^{-1} in the CFSm5

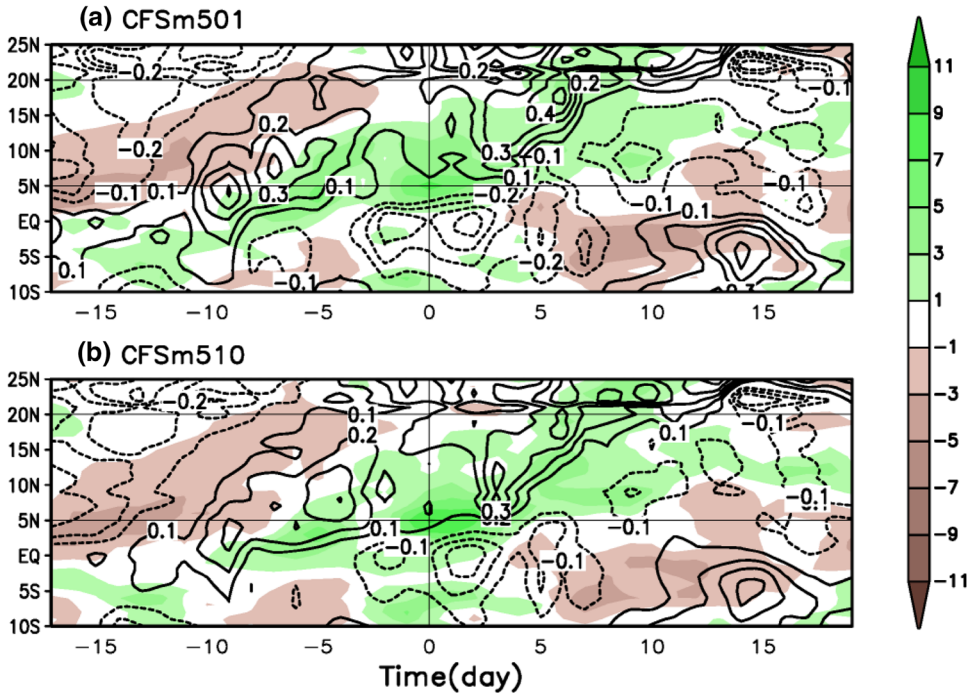

Fig. 8 Hovemoller plots of rainfall rate anomalies (unit: mm day^{-1}, shaded) and SST anomalies (unit: K, contour) averaged over between 65° and 95°E from composite **a** CFSm501 runs and **b** CFSm510 runs of the three strong MISO events at 11-day lead forecast

forecast, and over 9 mm day^{-1} in the CMORPH observation between 5°N and 20°N. The standard deviation of 11-day lead forecast of intraseasonal SST and rainfall anomalies are also compared between the two CFSm5 experiments (figures not shown). The CFSm501 generally produces larger variation of intraseasonal SST anomalies than the CFSm510 does, especially in the northern Indian Ocean.

Observational and forecast intraseasonal rainfall anomalies averaged over the northern Indian Ocean (5°–20°N, 65°–95°E) are examined in Fig. 9a, b. Figure 9a presents the regional averaged intraseasonal rainfall from the CMORPH observation and CFSm5 and GFS 1-day lead forecast. Due to the impact of the same initial conditions for all numerical experiments, CFSm5 and GFS forecasts overall reproduce the phase and amplitude of observational rainfall. However, the models overestimated the negative rainfall anomaly before Day − 4 and missed the observed initial development of the positive rainfall anomalies around Day − 5. In addition, the models overestimated positive rainfall anomalies from Day 7 to 12. These forecast errors possibly indicate the limits of the capability of the forecast system with the given observational analyses for initial conditions and oceanic surface boundary conditions.

For the forecast at the 11-day lead (Fig. 9b) when the impact of the atmospheric initial memory is less and the SST boundary conditions become more important, the regionally-averaged maximum rate from all CFSm5 and GFS runs are approximately 3 mm day^{-1}, which is less than half of the CMORPH observation. Among the numerical forecasts, both coupled model experiments (CFSm501 and CFSm510) produced more reasonable initiation of positive rainfall anomalies from Day − 4 to Day 2 than the atmosphere-only experiments (GFS_SSTdly and GFS_SSTssn) with the CFSm501 being closer to the observation than the CFSm510. The start of the development of positive rainfall anomalies in the GFS_SSTssn around Day 0 was delayed by 6 days compared to Day − 6 in the observation and CFSm501.

The observational and 11-day lead forecasts of intraseasonal SST anomalies averaged in (5°–20°N, 65°–95°E) are shown in Fig. 9c. As expected, the SST from GFS_SSTdly overlaps with the observed, because it is forced with the observational SST; GFS_SSTssn forecast is near 0 due to the use of SSTs without intraseasonal variations. Both CFSm5 experiments capture the overall warming tendency in the observational SST before Day − 10. However, the CFSm5 experiments delay the observed cooling tendency after Day 0, which is probably related to the weaker positive rainfall anomalies before Day 4. The magnitude of intraseasonal SST anomalies is overestimated in both CFSm5 forecasts as shown in the Fig. 8. Overall, CFSm501 forecast is slightly closer to observation than CFSm510. Although CFSm5 forecast presents biases in intraseasonal SST prediction, the forecast of intraseasonal rainfall by CFSm5 is still better than two GFS forecasts. This improvement in intraseasonal rainfall forecast in CFSm5 is thus mainly attributed to the inclusion of a dynamic ocean in the CFSm5.

Therefore, between the two CFSm5 forecast, the CFSm501 has a slightly but consistently better performance in the location of rainfall band and its northward propagation

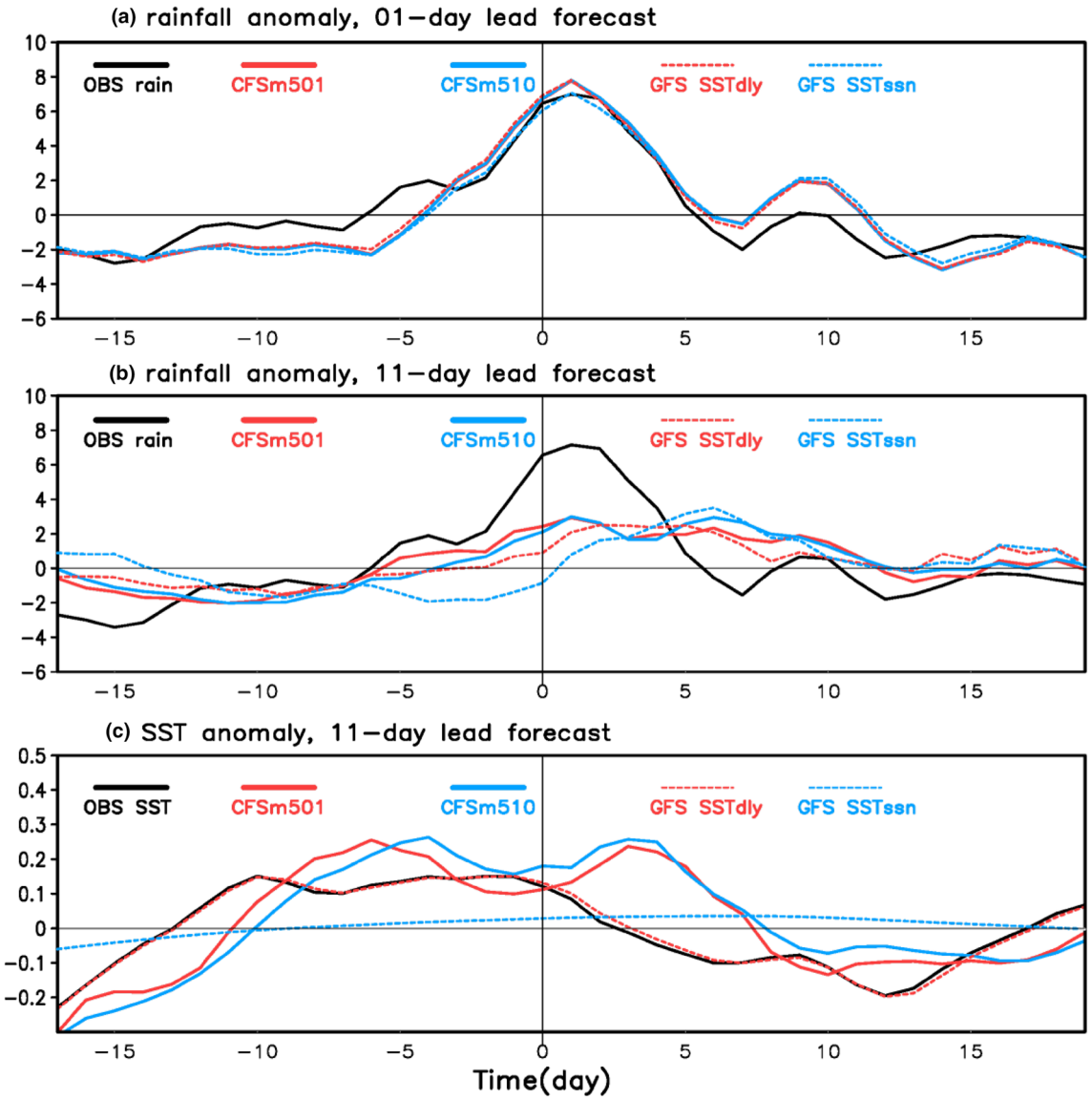

Fig. 9 Rainfall rate anomalies (unit: mm day^{-1}) and SST anomalies (unit: K) averaged over (5°–20°N, 65°–95°E) from observations and composite GFS and CFSm5 forecasts of the three strong MISO events. **a** Rainfall anomalies at 01-day lead forecast; **b** rainfall rate anomalies at 11-day lead forecast; and **c** SST anomalies at 11-day lead forecast

speed than the CFSm510 does. This improvement in the intraseasonal rainfall forecast in CFSm501 results from the high vertical resolution in the upper ocean and the induced larger amplitude of intraseasonal SST anomaly than that in the CFSm501. In addition, due to the inclusion of air–sea interaction, CFSm5 experiments show better prediction in intraseasonal rainfall than all GFS runs, even though the predicted SSTs includes errors due to inaccurate response in atmospheric convection and the related surface fluxes.

Differences in the relationships among SST, precipitation, and LHF were calculated to assess the impact of air–sea interactions. As the lead time increases, the effect of atmospheric initial memory decays and the relationships between LHF and SST, and between SST and precipitation become less realistic in uncoupled predictions (not shown): (1) in observations and coupled forecast (CFSm501), the reduction in LHF loss is leading the warm SST anomalies, implying that the SST varies in response to LHF changes, while in GFS_SSTdly, the air–sea interactions are opposite, i.e., LHF is in response to SST; and (2) the SST-precipitation variation becomes more simultaneous in GFS_SSTdly.

These relationship differences between coupled and uncoupled predictions are consistent with results from previous studies (Woolnough et al. 2000; Inness and Slingo 2003; Fu et al. 2007; Pegion and Kirtman 2008). However, when compared to observations, all experiments look more

similar to each other than any one of them does to observations (Fig. 9b). This may suggest that the coupling or SST variability has only small incremental impact on the MISO prediction skill. The common biases in the experiments with different treatment for SST indicate that parameterizations of other processes such as convection-largescale circulation interaction and cloud-radiation interaction in the atmosphere in the model also have strong influences. Convection schemes have been shown to be important in simulating the tropical intraseasonal oscillation (Wang et al. 2015). Cloud-radiation feedback has also been suggested to be a driving factor in the development of the MJO (Kim et al. 2015; Del Genio and Chen 2015). Del Genio (2015) showed that vertical distribution of radiative heating rate has well-defined structures that vary with MJO phases and geographical regions. In particular, Kim et al. (2015) found that the magnitude of anomalous radiative heating in moderately precipitating phases of the MJO differentiates the performance of MJO simulations in general circulation models (GCMs) with models that simulate stronger MJO also simulate a greater greenhouse enhancement factor. While the focus of this study is on the representation of the SST on the MISO prediction, further studies will be required to evaluate the cloud-radiation feedback in the model for improving MISO and MJO predictions.

5 Discussion and conclusions

This study investigated the impact of different specifications of the underlying SST on the prediction of intraseasonal rainfall associated with strong MISO events in the northern Indian Ocean. A series of GFS forecast experiments forced with hourly, daily, and seasonal observational SSTs were performed for the prediction of the selected three strong MISO events. The comparison between these GFS forecasts shows that SST intraseasonal variability was more important than its diurnal and seasonal variability in the MISO prediction. The GFS experiments forced with daily-mean SSTs, which included intraseasonal variability, had faster speed in the northward propagation of the MISO intraseasonal rainfall anomalies and higher prediction skill than those forced with seasonal SSTs which did not include intraseasonal variability. No significant difference was found in the GFS MISO prediction between the experiment forced with hourly SSTs and that with daily-mean SSTs. The GFS run forced with warmer and colder seasonal SST show similar prediction skill in the MISO prediction, suggesting that the mean SST state was not a crucial factor in the MISO evolution.

To further investigate the role of the ocean surface condition, experiments with a coupled atmosphere–ocean model were carried out using two different vertical resolutions for the upper ocean. The CFSm501 with 1-m vertical resolution in the upper ocean had a higher prediction skill in both intraseasonal SST and rainfall and closer to observations than CFSm510 with a typical 10-m vertical resolution in the upper ocean. The better performance in the CFSm501 forecast stems from the better resolving oceanic processes due to the finer vertical resolution in the upper ocean. Compared to GFS experiments, both CFSm5 experiments (CFSm501 and CFSm510) had higher prediction skills for rainfall variability than all GFS experiments including those forced with hourly and daily OSTIA SSTs, although SSTs in CFSm5 experiments contained sizeable errors. It suggests that both SST intraseasonal variability and air–sea interaction were important factors in the MISO prediction. One deficiency in all GFS and CFSm5 forecasts is the underestimation of the amount of positive intraseasonal rainfall anomaly. As shown in the Fig. 8, both GFS and CFSm5, which are initialized from the same CFSR states, have the capability to forecast the intraseasonal rainfall at 1-day lead at its peak phase but delay the initial development of rainfall anomaly onset by a few days. As the lead time increase beyond a week, the GFS cannot produce the right amount of positive intraseasonal rainfall anomaly at the observed peak phase. The inclusion of air–sea coupling processes in the CFSm5 helps correct the phase of rainfall but only slightly improves the amplitude. Hence, the deficiency of weak rainfall anomalies mainly results from the limit of rainfall forecast in GFS, which is probably due to the uncertainty in the convection in the GFS. The RAS convection scheme used in this study has been shown to be the most skillful in reproducing intraseasonal rainfall anomalies among three optional convection schemes in the NCEP models (Wang et al. 2015). Our analysis in this study suggests that further validation of the convection schemes in GFS, including RAS, is required for an improved intraseasonal rainfall prediction.

Given the unsatisfactory performance in the prediction of intraseasonal SST, there is still room for improvement in the CFSm5. In this study, the two CFSm5 models (CFSm501 and CFSm510) are initialized from the same CFSR states for both atmosphere and ocean. Another option for oceanic initial conditions is the output from long-term simulations by MOM5 with 1-m and the typical 10-m vertical resolutions in the upper ocean as in Ge et al. (2017). The use of oceanic initial conditions from the ocean simulations with 1-m vertical oceanic forced by surface fields from an atmospheric reanalysis may lead to an additional enhancement of MISO prediction skill.

Acknowledgements The authors greatly appreciate the helpful reviews by Zeng-Zhen Hu and Jieshun Zhu, and the anonymous reviewers. We thank Jieshun Zhu for his help with the revision of the manuscript. Ying Zhang gratefully acknowledges the financial support given by the Earth System Science Organization, Ministry of Earth Sciences, Government of India, to conduct this research under the Monsoon Mission.

Ying Zhang is also supported by the NOAA Climate Program Office CVP program. The scientific results and conclusions, as well as any view or opinions expressed herein, are those of the author(s) and do not necessarily reflect the views of NWS, NOAA, or the Department of Commerce.

References

Bellenger H, Duvel J-P (2009) An analysis of tropical ocean diurnal warm layers. J Clim 22:3629–3646

Bernie DJ, Gullyardi E, Madec G, Slingo JM, Woolnough SJ (2007) Impact of resolving the diurnal cycle in an ocean-atmosphere GCM. Part 1: a diurnally forced OGCM. Clim Dyn 29:575–590

Bernie DJ, Gullyardi E, Madec G, Slingo JM, Woolnough SJ, Cole J (2008) Impact of resolving the diurnal cycle in an ocean-atmosphere GCM. Part 2: a diurnally forced CGCM. Clim Dyn 31:909–925

Davey M et al (2002) STOIC: a study of coupled model climatology and variability in tropical ocean regions. Clim Dyn 18:403–420. https://doi.org/10.1007/s00382-001-0188-6

de Szoeke SP, Edson JB, Marion JR, Fairall CW, Bariteau L (2015) The MJO and air–sea interaction in TOGA COARE and DYNAMO. J Clim 28:597–622

Del Genio AD (2015) Constraints on cumulus parameterization from simulations of observed MJO events. J Clim 28:6419–6442

Del Genio AD, Chen Y (2015) Cloud-radiative driving of the Madden–Julian oscillation as seen by the A-Train. J Geophys Res Atmos 120:5344–5356. https://doi.org/10.1002/2015JD023278

DeMott CA, Stan C, Randall DA (2013) Northward propagation mechanisms of the boreal summer intraseasonal oscillation in the ERA-Interim and SP-CCSM. J Clim 26:1973–1992

DeMott CA, Benedict JJ, Klingaman NP, Woolnough SJ, Randall DA (2016) Diagnosing ocean feedbacks to the MJO: SST-modulated surface fluxes and the moist static energy budget. J Geophys Res Atmos 121:8350–8373

Donlon CJ, Martin M, Stark J, Roberts-Jones J, Fiedler E, Wimmer W (2012) The operational sea surface temperature and sea ice analysis (OSTIA) system. Remote Sens Environ 116:140–158

Fu X, Wang B (2004) Differences of boreal summer intraseasonal oscillations simulated in an atmosphere–ocean coupled model and an atmosphere-only model. J Clim 17:1263–1271

Fu X, Wang B, Li T, McCreary JP (2003) Coupling between northward-propagating, intraseasonal oscillations and sea surface temperature in the Indian Ocean. J Atmos Sci 60:1733–1753

Fu X, Wang B, Waliser D, Tao L (2007) Impact of atmosphere–ocean coupling on the predictability of monsoon instraseasonal oscillations. J Atmos Sci 64:157–174

Fu X, Yang B, Bao Q, Wang B (2008) Sea surface temperature feedback extends the predictability of tropical intraseasonal oscillation. Mon Weather Rev 136:577–597

Fu X, Wang B, Bao Q, Liu P, Lee J-Y (2009) Impacts of initial conditions on monsoon intraseasonal forecasting. Geophys Res Lett 36:L08801. https://doi.org/10.1029/2009GL037166

Gadgil S, Rao PRS (2000) Farming strategies for a variable climate—a challenge. Curr Sci 78:1203–1215

Gao Y, Klingaman NP, Demott CA, Hsu P-C (2018) Diagnosing ocean feedbacks to the BSISO: SST-modulated surface fluxes and the moist static energy budget. J Geophys Res Atmos 124:146–170. https://doi.org/10.1029/2018JD029303

Ge X, Wang W, Kumar A, Zhang Y (2017) Importance of the vertical resolution in simulating SST diurnal and intraseasonal variability in an oceanic general circulation model. J Clim 30:3963–3978. https://doi.org/10.1175/JCLI-D-16-0689.1

Goswami BN, Ajayamohan RS (2001) Intraseasonal oscillation and interannual variability of the Indian summer monsoon. J Clim 14:1180–1198

Griffies SM (2012) Elements of the Modular Ocean Model (MOM) (2012 release): GFDL Ocean Group Tech. Rep. No. 7. NOAA/Geophysical Fluid Dynamics Laboratory

Inness PM, Slingo JM (2003) Simulation of the Madden–Julian Oscillation in a coupled general circulation model. Part I: comparisons with observations and an atmosphere-only GCM. J Clim 16:345–364

Inness PM, Slingo JM, Guilyardi E, Cole J (2003) Simulation of the Madden–Julian oscillation in a coupled general circulation model. Part II: The role of the basic state. J Clim 16:365–382

Joyce RJ, Janowiak JE, Arkin PA, Xie P (2004) CMORPH: a method that produces global precipitation estimates from passive microwave and infrared data at high spatial and temporal resolution. J Hydrometeorol 5:487–503

Kemball-Cook SR, Weare BC (2001) The onset of convection in the Madden–Julian oscillation. J Clim 14:780–793

Kim D, Ahn M-S, Kang I-S, Del Genio AD (2015) Role of longwave cloud-radiation feedback in the simulation of the Madden–Julian Oscillation. J Clim 28(17):6979–6994. https://doi.org/10.1175/JCLI-D-14-00767.1

Klingaman NP, Inness PM, Weller H, Slingo JM (2008a) The importance of high-frequency sea surface temperature variability to the intraseasonal oscillation of Indian monsoon rainfall. J Clim 21:6119–6140

Klingaman NP, Weller H, Slingo JM, Innes PJ (2008b) The intraseasonal variability of the Indian summer monsoon using TMI sea-surface temperatures and ECMWF reanalysis. J Clim 21:2519–2539

Klingaman NP, Woolnough SJ, Weller H, Slingo JM (2011) The impact of finer-resolution air–sea coupling on the intraseasonal oscillation of the Indian monsoon. J Clim 24:2451–2468

Krishnamurti TN, Ardanuy P (1980) The 10 to 20-day westward propagating mode and "Breaks in the Monsoons". Tellus 32:15–26

Krishnamurti TN, Subrahmanyam D (1982) The 30-50-day mode at 850 mb during MONEX. J Atmos Sci 39:2088–2095

Krishnamurti TN, Osterhof DK, Mehta AV (1988) Air–sea interaction on the time scale of 30 to 50 days. J Atmos Sci 45:1304–1322

Lau K-M, Chan PH (1986) Aspects of the 40–50 oscillation during the northern summer as inferred from the outgoing longwave radiation. Mon Weather Rev 14:1354–1367

Lawrence DM, Webster PJ (2002) The boreal summer intraseaonal oscillation: relationship between northward and eastward movement of convection. J Atmos Sci 59:1593–1606

Li G, Xie S-P, Du Y (2015) Monsoon-induced biases of climate models over the tropical Indian Ocean. J Clim 28:3058–3072

Li Y, Han W, Wang W, Ravichandran M (2016) Intraseasonal variability of SST and precipitation in the Arabian Sea during the Indian Summer Monsoon: impact of ocean mixed layer depth. J Clim 29:7889–7910

Moorthi, S., and M. J. Suarez, 1999: Documentation of version 2 of relaxed Arakawa–Schubert cumulus parameterization with convective downdrafts. NOAA Tech. Note NWS/NCEP 99-01

Moorthi S, Suarez MJ (1992) Relaxed Arakawa–Schubert: a parameterization of moist convection for general circulation models. Mon Weather Rev 120:978–1002. https://doi.org/10.1175/1520-0493(1992)120%3c0978:RASAPO%3e2.0.CO;2

Murakami M (1976) Analysis of summer monsoon fluctuations over India. J Meteorol Soc Jpn 54:15–31

Pan H-L, Wu W-S (1995) Implementing a mass flux convection parameterization package for the NMC medium-range forecast model. NMC Office Note 409

Pegion K, Kirtman B (2008) The impact of air–sea interactions on the simulation of tropical intraseasonal variability. J Clim 21:6616–6635

Roxy M, Tanimoto Y (2007) Role of SST over the Indian Ocean in influencing the intraseasonal variability of the Indian summer monsoon. J Meteorol Soc Jpn 85:349–358

Saha S et al (2006) The NCEP Climate Forecast System. J Clim 19:3483–3517

Saha S et al (2010) The NCEP Climate Forecast System reanalysis. Bull Am Meteorol Soc 91:1015–1057

Saha S et al (2014) The NCEP Climate Forecast System version 2. J Clim 27:2185–2208. https://doi.org/10.1175/JCLI-D-12-00823.1

Seo K-H, Schemm J-KE, Wang W, Kumar A (2007) The boreal summer intraseasonal oscillation simulated in the NCEP Climate Forecast System: the effect of sea surface temperature. Mon Weather Rev 135:1807–1827

Seo H, Subramanian AC, Miller AJ, Cavanaugh NR (2014) Coupled impacts of the diurnal cycle of sea surface temperature on the Madden–Julian oscillation. J Clim 27:8422–8443. https://doi.org/10.1175/jcli-d-14-00141.1, https://hdl.handle.net/1912/6996

Suhas E, Neena JM, Goswami BN (2013) An Indian monsoon intraseasonal oscillations (MISO) index for real time monitoring and forecast verification. Clim Dyn 40:2605–2616

Tseng W-L, Tsuang B-J, Keelyside NS, Hsu H-H, Tu C-Y (2014) Resolving the upper-ocean warm layer improves the simulation of the Madden–Jullian oscillation. Clim Dyn 44:1487–1503

Wang B, Rui H (1990) Synoptic climatology of transient tropical intraseasonal convection anomalies: 1975–1985. Meteorol Atmos Phys 44:43–61

Wang B, Xie X (1997) A model for the boreal summer intraseasonal oscillation. J Atmos Sci 54:72–86

Wang B, Xie X (1998) Coupled modes of the warm pool climate system. Part I: the role of air–sea interaction in maintaining Madden–Julian Oscillation. J Clim 11:2116–2135

Wang W, Chen M, Kumar A (2009) Impacts of ocean surface on the northward propagation of the boreal summer intraseasonal oscillation in the NCEP Climate Forecast System. J Clim 22:6561–6576. https://doi.org/10.1175/2009JCLI3007.1

Wang C, Zhang L, Lee S-K, Wu L, Mechoso CR (2014) A global perspective on CMIP5 climate model biases. Nat Clim Change 4:201–205. https://doi.org/10.1038/nclimate2118

Wang W, Kumar A, Fu J, Hung M-P (2015) What is the role of the sea surface temperature uncertainty in the prediction of tropical convection associated with the MJO? Mon Weather Rev 143:3156–3175. https://doi.org/10.1175/MWR-D-14-00385.1

Webster PJ et al (1998) Monsoons: processes, predictability and the prospects of prediction. J Geophys Res 103:14451–14510

Woolnough SJ, Slingo JM, Hoskins BJ (2000) The relationship between convection and sea surface temperature on intraseasonal timescales. J Clim 13:2086–2104

Woolnough SJ, Vitart F, Balmaseda MA (2007) The role of the ocean in the Madden–Julian Oscillation: implications for MJO prediction. Q J R Meteorol Soc 133:117–128

Yasunari T (1979) Cloudiness fluctuation associated with the Northern Hemisphere summer monsoon. J Meteorol Soc Jpn 57:227–242

Yasunari T (1980) A quasi-stationary appearance of 30- to 40-day period in the cloudiness fluctuations during the summer monsoon over India. J Meteorol Soc Jpn 58:225–229

Zhu J, Wang W, Kumar A (2017) Simulations of MJO propagation across the Maritime Continent: impacts of SST feedback. J Clim 30:1689–1704. https://doi.org/10.1175/JCLIM-D-16-0367.1